Supporting Information

Van Eps et al. 10.1073/pnas.1721896115

SI Materials and Methods

Refinement of the Experimental Model. Before performing MD simulations of the rhodopsin–G_i complex, we performed several steps of structural refinement of the DEER-based model. We first generated a complete model of the complex. The DEER-modeled complex was aligned on the transmembrane helices of the Orientations of Proteins in Membranes database structure for PDB ID code 4ZWJ (31). Next, residues Cys322 and Cys323 of rhodopsin were palmitoylated. The N terminus of the $G\alpha_i$-subunit was extended by three residues to include residues 2 to 4 and a palmitoyl was added to Cys3, required for maintaining stable membrane insertion of G_i. The backbone dihedrals in the vicinity of Cys3 were manually adjusted to obtain an orientation that allowed for its proper insertion into the bilayer. Finally, the C terminus of the Gγ-subunit was extended to include residues 61 to 68, using atomic coordinates modeled in ref. 34.

All spin-labeled cysteine residues were back-mutated to their wild-type identities. The receptor model in the simulations lacked the retinal ligand, the presence of which increases the thermostability of the protein. A disulfide bond between mutations N2C and D282C was thus introduced to effectively offset the loss of stability due to the absence of retinal ligand (48, 49). Prime (Schrödinger) was used to add hydrogens and cap all protein termini, except for the $G\alpha_i$ C terminus, which retained a complete carboxylate moiety. Residues Asp83, Glu113, and Glu122 were protonated in accordance with evidence that these residues are protonated in activated forms of rhodopsin (47). Other titratable residues were left in their dominant protonation state at pH 7.0. All histidine residues retained a hydrogen on the epsilon nitrogen, unless shifting it to the delta nitrogen helped to optimize the local hydrogen-bonding network. Prime was also used to fill in missing residues in the G protein (A326 to K330). The helical domain (residues 60 to 182) was not included in the refined model, because no experimental distance measurements were carried out on this portion of the complex, and earlier simulations of the β_2AR–G_s complex demonstrated that the helical domain fluctuated substantially (34).

The Minimize tool in Maestro (Schrödinger) was then used to reduce clashes between residues at the rhodopsin–$G\alpha_i$ interface. Subsequent minimization was carried out on the entire protein complex to further reduce clashes introduced upon addition of hydrogens.

We note that the simulations lacked certain features that might help to further stabilize the complex. In terms of lipid modifications, the simulations lacked the prenylation of the Gγ-subunit and the *N*-myristoylglycine on residue 2 of $G\alpha_i$. The latter apparently facilitates protein expression and trafficking, but evidence suggests the palmitoylcysteine adjacent to it plays a greater role in membrane localization (52). The simulations also lacked the helical domain, whose presence might otherwise help to constrain motion of the Ras-like domain. Finally, in the simulations, the second intracellular loop of rhodopsin lacks a helical secondary structure, a conformation that might aid in stabilization of the rhodopsin–$G\alpha_i$ interface.

System Preparation for MD Simulation. The prepared protein complex was inserted into a preequilibrated palmitoyl-oleoyl-phosphatidylcholine bilayer using Dabble, a membrane protein preparation software (53). The final system dimensions were $103 \times 129 \times 174$ Å^3, including 327 lipids, 57,446 water molecules, ∼156 sodium ions, and 146 chloride ions.

MD Simulation Force Field Parameters. The CHARMM36m parameter set was employed for protein molecules, the CHARMM36 parameter set for lipids and salt, and the CHARMM36 TIP3P model employed for water (50, 54). Parameters for the custom residue palmitoylcysteine were generated using the ParamChem webserver and the CGENFF parameter set (55–57).

MD Simulation Protocols. MD simulations were performed on GPUs with the CUDA version of PMEMD (particle mesh Ewald molecular dynamics) in AMBER16 (51, 58). Each system underwent minimization followed by heating using the Langevin thermostat from 0 to 100 K in the NVT ensemble over 12.5 ps with harmonic restraints of 10.0 kcal·mol^{-1}·Å^{-2} on the nonhydrogen atoms of lipid, protein, and ligand, with initial velocities sampled from the Boltzmann distribution. Next, each system was heated to 310 K over 125 ps in the NPT ensemble with semiisotropic pressure coupling and a pressure of 1 bar. Subsequent equilibration was performed at 310 K with harmonic restraints applied to the protein starting at 5.0 kcal·mol^{-1}·Å^{-2} and reduced in strength by 1.0 kcal·mol^{-1}·Å^{-2} in a stepwise fashion every 2 ns for 10 ns and then by 0.1 kcal·mol^{-1}·Å^{-2} in a stepwise fashion every 2 ns for 20 ns, for a total of 30 ns of additional restrained equilibration. Each of three independent production runs lasted ∼600 ns. Production simulations were conducted at 310 K and 1 bar in the NPT ensemble, using a Langevin thermostat and Monte Carlo barostat.

Simulations employed a time step of 4.0 fs with hydrogen mass repartitioning (59). Simulations were performed with periodic boundary conditions, and bond lengths to hydrogen atoms were constrained with SHAKE (60). van der Waals and short-range electrostatic interactions were cut off at 9.0 Å, and long-range electrostatic interactions were computed using the particle mesh Ewald method with a Ewald coefficient β of ∼0.31 Å and B-spline interpolation of order 4. The fast Fourier transform (FFT) grid size was chosen such that the width of a grid cell was ∼1 Å.

A trajectory snapshot was saved every 200 ps during production simulations. The AmberTools15 CPPTRAJ package was used to reimage and center trajectories (61), and simulations were visualized and analyzed using VMD (62).

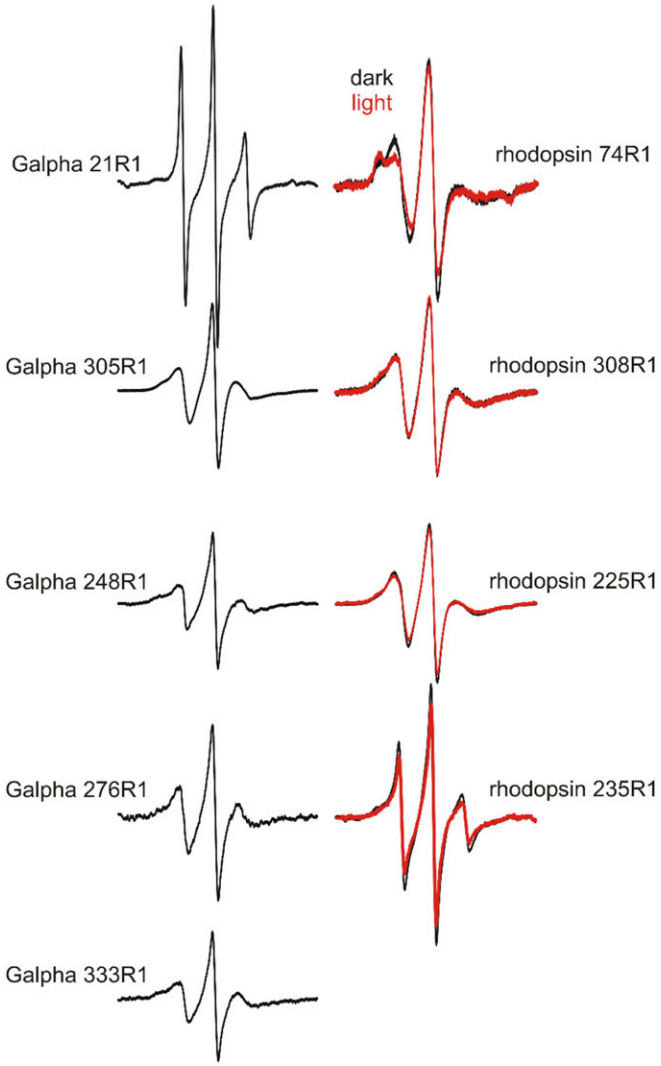

Fig. S1. Continuous-wave (CW) EPR spectra of spin-labeled $G\alpha_i$ and rhodopsin mutants. Spectra are 100-Gauss scans which have been normalized for comparison purposes. For rhodopsin, both dark and light-activated spectra are shown. For all sites selected in the G protein the spectra are consistent with solvent-exposed surface sites on the protein. Except for site 74, located at a helix–helix contact, the same is the case for rhodopsin. Moreover, light activation produces only minor changes in the CW EPR spectra for rhodopsin mutants, indicating that local structural changes are not significant in the vicinity of these sites. Thus, changes in interspin distances for pairs involving these sites are the result of global structural rearrangement.

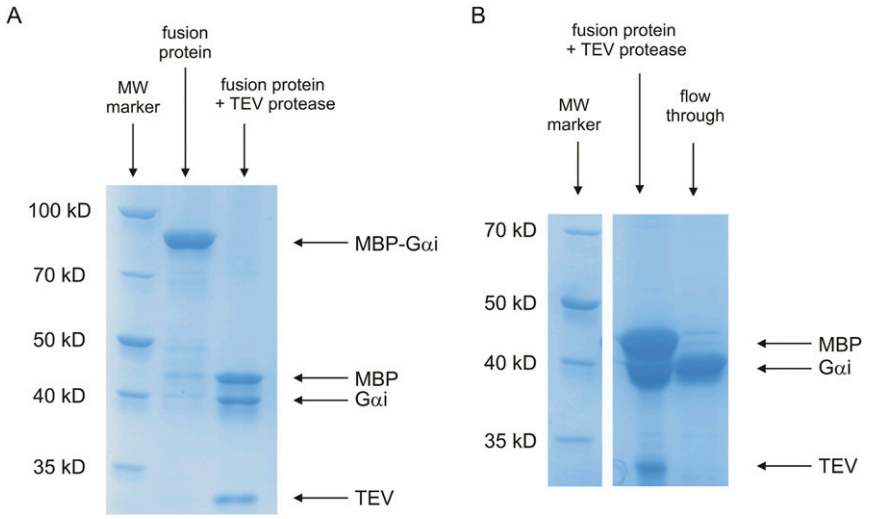

Fig. S2. Representative Coomassie blue-stained SDS/PAGE of a $G\alpha_i$ cysteine mutant (276C). (*A*) Polyacrylamide gel showing the MBP–$G\alpha_i$ fusion before and after cleavage by TEV protease. Upon cleavage of the fusion, MBP, $G\alpha_i$, and TEV protease bands are observed on the gel at ~45, 40, and ~25 kDa, respectively. (*B*) Gel showing the purification of the $G\alpha_i$-fragment. The cleavage mixture was passed over an Ni^{2+}-NTA column and the nonretained fractions containing the $G\alpha_i$-subunit were collected. Lane 1 shows the cleavage mixture, while lane 2 shows a flow-through fraction. Flow-through fractions were pooled for spin labeling. Similar purity was observed for other $G\alpha_i$ cysteine mutants.

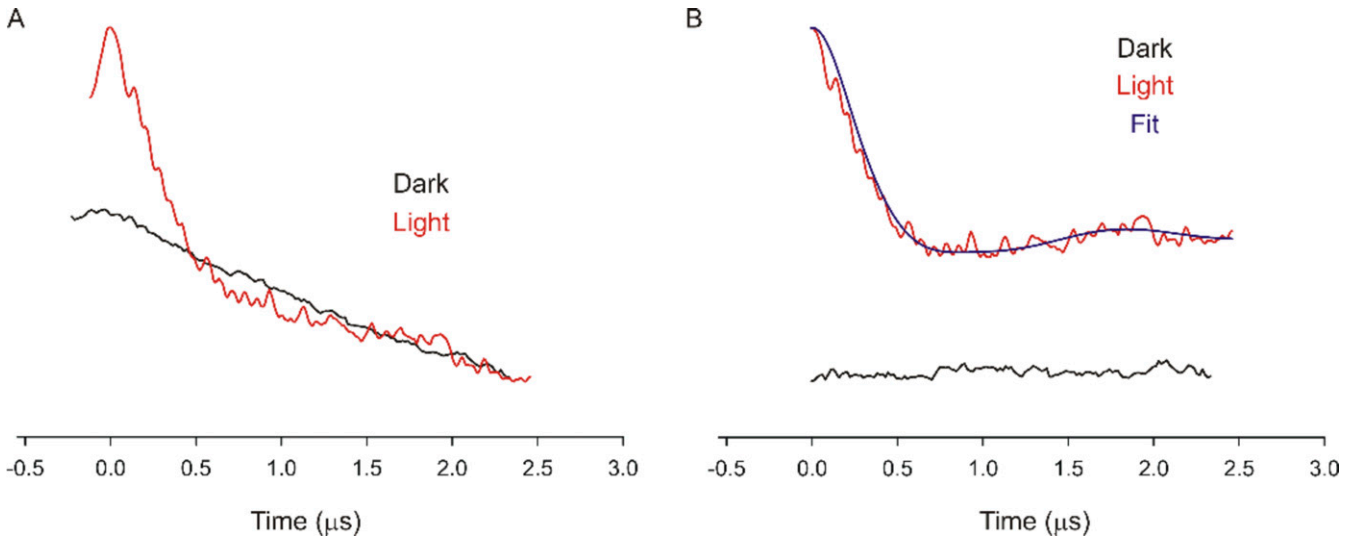

Fig. S3. Light-dependent changes in DEER signals illustrate ternary complex formation. Example of Rho225R1–$G\alpha_i$305R1$\beta\gamma$ measurement in the dark (black trace) and after light activation of rhodopsin (red trace). (*A*) The raw DEER data show changes in the DEF upon ternary complex formation between Rho225R1 and $G\alpha_i$305R1$\beta\gamma$. (*B*) Background-corrected DEFs from *A*. The blue trace is a fit to the data of the measurement after light activation. The red trace has a modulation depth of 0.15.

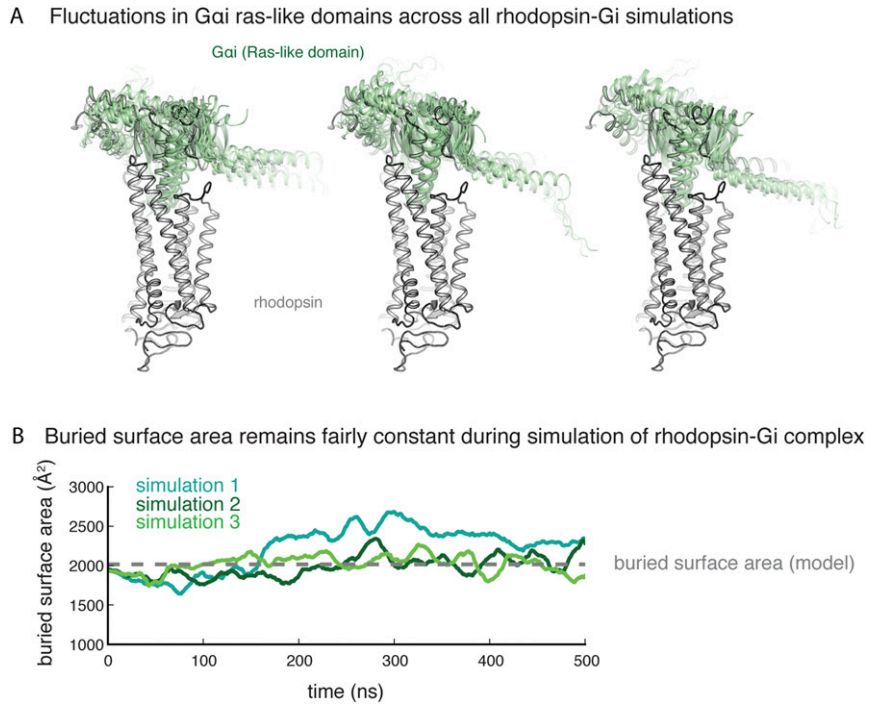

Fig. S4. Evaluation of rhodopsin–$G\alpha_i$ complex stability in MD simulations. (*A*) Snapshots were extracted from rhodopsin–$G\alpha_i$ complex simulations (every 54 ns between 0 and 500 ns of production simulation, with the frames in the first 100 ns removed to account for complex relaxation, for each of three simulations in this manuscript) and displayed as in Fig. 3. The overall orientation of $G\alpha_i$ relative to the receptor remains constant in simulation. (*B*) Calculation of buried surface area between rhodopsin and $G\alpha_i$ for three independent simulations reveals that buried surface area remains fairly constant. The gray dashed line indicates the buried surface area formed in the original, refined complex.

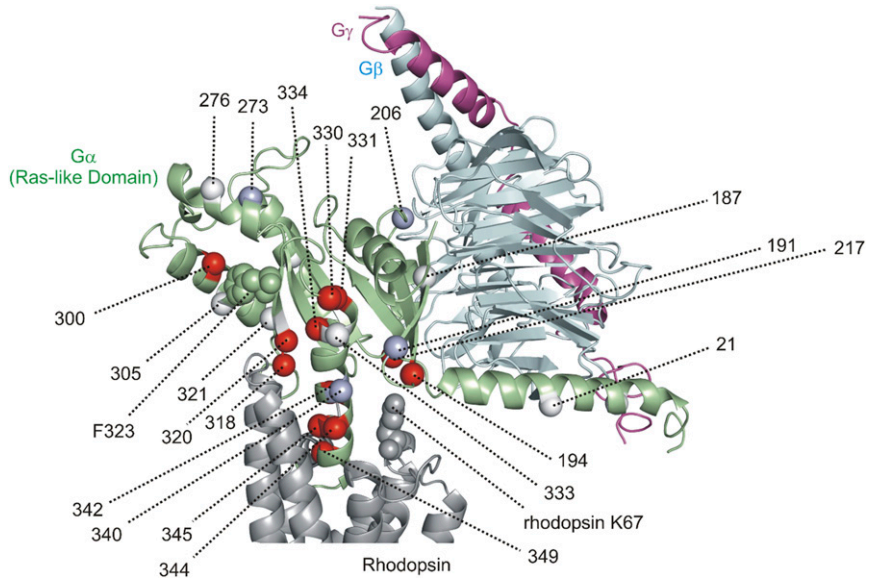

Fig. S5. CW EPR spectral changes of spin-labeled $G\alpha_i$ mutants upon binding to rhodopsin (23–25, 33). Cα-carbon spheres at each $G\alpha_i$ spin-labeling site are plotted on top of the model. The spheres are color-coded to represent increases in nitroxide mobility upon receptor binding (light blue), no change in nitroxide mobility upon receptor binding (white), or a decrease in nitroxide mobility upon receptor binding (red). Site F323 on $G\alpha_i$ is shown as green spheres to illustrate the proximity of this residue to site 300 on helix 4 of $G\alpha_i$. Subtle conformational changes in the β6-sheet propagate to a spin label placed at site 300. Rhodopsin K67 is shown as gray spheres. This site lies in proximity to a spin-labeled $G\alpha_i$ 217R1 mutant. Steric contact between these sites leads to immobilization of the nitroxide (33).

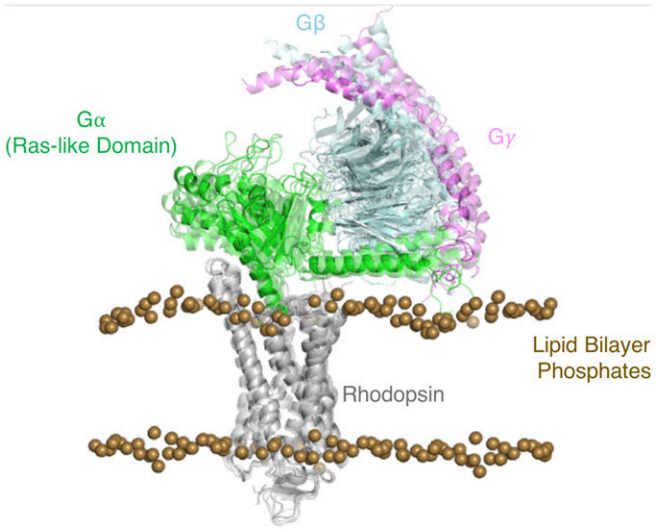

Fig. S6. Fluctuations observed across the entire rhodopsin–G_i complex in MD simulation. Simulation snapshots representing every 150 ns from simulation 1 of this paper are overlaid on top of the refined DEER model. Simulations also reveal large fluctuations in the Gβ- and Gγ-subunits; the orientation of these subunits relative to the remainder of the complex was not mapped through DEER studies.

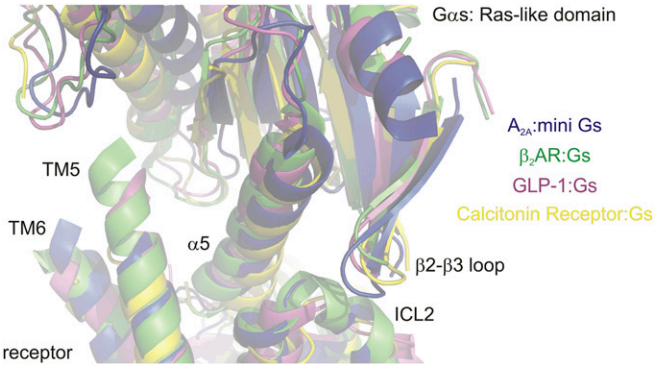

Fig. S7. Structural overlay of GPCR–G_s complexes. Shown are the crystal structures of the β_2AR–G_s complex [green; PDB ID code 3SN6 (12)] and the adenosine A_{2A} receptor–mini-G_s complex [blue; PDB ID code 5G53 (11)], as well as the cryoelectron microscopy structures of the calcitonin receptor–G_s complex [yellow; PDB ID code 5UZ7 (14)] and the GLP-1 receptor–G_s complex [magenta; PDB ID code 5VAI (13)]. Only the cytoplasmic surfaces of each receptor and the Ras-like domains of the $G\alpha_s$-subunits are shown for clarity. TM6, TM5, and intracellular loop 2 (ICL2) of the receptor are denoted along with the α5-helices and β2–β3 loops of the $G\alpha_s$ Ras-like domains.